

High-resolution He I 10830 Å Narrowband Imaging for an M-class Flare. III. EUV Late Phase

Ya Wang ^{1,2}, Haisheng Ji^{1,3}, Alexander Warmuth⁴, Ying Li¹, and Wenda Cao⁵

¹ Key Laboratory of Dark Matter and Space Astronomy, CAS, Nanjing 210023, People's Republic of China; wangya@pmo.ac.cn

² Key Laboratory for Modern Astronomy and Astrophysics (Nanjing University), Ministry of Education, Nanjing 210023, People's Republic of China

³ School of Astronomy and Space Science, University of Science and Technology of China, Hefei 230026, People's Republic of China

⁴ Leibniz-Institut für Astrophysik Potsdam (AIP), An der Sternwarte 16, D-14482 Potsdam, Germany

⁵ Big Bear Solar Observatory, Big Bear City, CA 92314, USA

**Received 2020 September 29; revised 2020 October 19; accepted 2020 October 21; published 2020 December 21

Abstract

In this paper, we report the EUV late phase for the M1.8 class flare on 2012 July 5 in the active region (AR) 11515. The late phase is shown by the prominent appearance of EUV emission at 131 Å of two additional flare loop systems (flare arcades 2 and 3, as named in this paper) other than the main flare loop (flare arcade 1), as observed by the Atmospheric Imaging Assembly (AIA) on board the Solar Dynamic Observatory (SDO). Three sets of flare arcades connect four flare ribbons, which forms an asymmetric quadrupole magnetic field configuration. While the emission from flare arcade 2, linking the pair of secondary flare ribbons, and arcade 3, linking one of the main flare ribbons and one of the secondary flare ribbons, conjointly contributes to the EUV late phase, their heating mechanisms are quite different. While the brightening of flare arcade 2 is the result of disturbance created by the eruption of EUV hot channels to the overlying coronal magnetic field, the heating of flare arcade 3 was closely associated with two rapid contractions of the overlying filament threads during the partial eruption of the filament. The contractions are discernible in He I 10830 Å images and have signatures in the EUV wavelengths of AIA. The two rapid contractions are the result of a sudden drop in magnetic pressure after the eruption of two hot channels. Clear evidence suggests that magnetic reconnection may occur between the contracting filament threads and the low-lying magnetic field.

Unified Astronomy Thesaurus concepts: Solar flares (1496); Solar extreme ultraviolet emission (1493); Solar filaments (1495)

Supporting material: animations

1. Introduction

Solar flares are among the most prominent explosive energy release phenomena in the solar system. During the flaring process, magnetic energy is rapidly converted into radiation from radio to extreme ultraviolet (EUV), X-ray, and sometimes even gamma-rays, high-energy particles, and coronal mass ejections (CME; e.g., Priest & Forbes 2002; Schrijver 2009; Fletcher et al. 2011). They reach Earth in several minutes, hours, or couple of days, posing various safety hazards to space weather. The classification of solar flares is primarily made according to the peak brightness of Soft X-ray (SXR) in the wavelength range 1-8 Å. According to the temporal profile of the SXR emission, flaring processes are divided into pre-flare phase, impulsive phase, and gradual phase (or decay phase), and the impulsive phase was usually regarded as the most important phase for energy release. The gradual phase had attracted less attention until Woods et al. (2011) revealed that it sometimes contains a second peak in the warm EUV irradiance, e.g., Fe XVI 33.5 nm (\sim 3 MK). The second EUV peak was named as the EUV late phase (ELP), which is one of the major achievements made by the EUV Variability Experiment (EVE; Woods et al. 2012) on board the Solar Dynamics Observatory (SDO; Pesnell et al. 2012). Since the significant enhancement of EUV emission radiated during flares has a crucial impact on the Earth's ionosphere and thermosphere (Kane & Donnelly 1971; Donnelly & Kane 1978), the study of ELP is very important not only for investigating how magnetic energy is

converted during the phase but also for constructing the ionosphere-thermosphere models during flares.

Much progress has been made by a variety of studies regarding the physics of the ELP. Some basic facts from observation have been made clear. We have learned that ELP events are frequently associated with a complex multipolar magnetic configuration or fan-spine magnetic topology (Woods et al. 2011). Commonly, the associated overlying coronal magnetic field usually consists of two sets of loops of different sizes with short loops connecting main flare ribbons and long loops (sometimes as a spine) connecting remote secondary flare ribbons (Li et al. 2014; Dai & Ding 2018a; Chen et al. 2020). It was proposed that the ELP is the result of a long-lasting cooling process of the longer late-phase loops, which are originally energized during the main phase (Liu et al. 2013; Sun et al. 2013; Dai et al. 2018b). However, many ELP events are obviously associated with the secondary heating in the gradual phase (Hock et al. 2012; Dai et al. 2013). For example, Liu et al. (2015) reported a case study, in which the second peak is \sim 2.1 stronger than the first peak at EUV 33.5 nm. It was attributed to the failed eruption of a hot channel, which continuously supplied thermal energy during the gradual phase and hence has led to the extremely large ELP. It was further revealed that the relative peaks of the noneruptive flares are systematically stronger than eruptive flares (Wang et al. 2016b). However, some ELP flares are definitely of eruptive nature starting from short loops and with both loop sets being disturbed (Woods et al. 2011). Details of the secondary heating processes during the flares are still insufficient, we need more

cases aided with high-resolution observations from a largeaperture groundbased telescope.

The active region NOAA 11515 and the adjoining active region 11514 were prolific in M- and C-class flares. One flare (SOL2012-07-05T21:38) was observed with high-cadence and high-spatial resolution narrowband imaging at He I 10830 Å. For the flare, we analyzed the interesting interaction between penumbra wave and one flare ribbon that sweeps into the penumbra of the active region's main sunspot. Meanwhile, we presented observational evidence for helium excitation by EUV irradiation directly with a time profile (Wang et al. 2016a). Moreover, by aligning with SDO/Atmospheric Imaging Assembly (AIA) EUV imaging data, we reported the evolution of multiple hot channels at EUV 131 Å, notably during the initiation process (Wang et al. 2018). After the eruption of the flux ropes, there appeared an ELP characterized by hot loops in the decay phase and a pair of secondary flare ribbons. In the present investigation, we focus on identifying the specific heating mechanism for the ELP. In Section 2, we give a description for the flare and observations, while results are presented in Section 3. A discussion and summary are given in Section 4.

2. The Data, the Active Region, and the Flare

As we introduced in the last section, the flare data (high-resolution He I 10830 Å narrowband (0.05 nm) images) were taken at the Big Bear Solar Observatory with the 1.6 m aperture Goode Solar Telescope (BBSO/GST; Goode et al. 2010). It was the first major flare observed by the GST. The cadence is about 10 s, with the pixel size of 0."0875 and a field of view (FOV) of $90'' \times 90''$. Besides, full-disk H α 6563 Å images routinely taken at BBSO are used to show the overview of the filaments and the remote flare ribbons, with the pixel size of \sim 1". Details about BBSO/GST data for the flare have also been described in the two preceeding papers (Wang et al. 2016a, 2018).

EVE measures the full-disk integrated EUV irradiance from 0.1 to 105 nm with spectral resolution of 0.1 nm and a cadence of 10 s (Woods et al. 2012). The EVE data used in this study is the EVE level-2 line data (EVL). AIA takes simultaneous fulldisk images in 10 passbands with the pixel size of 0."6 and a cadence of 12 s or 24 s (Lemen et al. 2012). The 10 passbands have different temperature response functions, six of which (94 Å, 131 Å, 171 Å, 193 Å, 211 Å, and 335 Å passbands) are sensitive to coronal temperatures. Besides, the 1600 Å passband (C IV+continuum, ~0.1 MK and 5000 K) images represent the emission from the transition region and the chromosphere, allowing us to trace the footpoint brightenings. A series of vector magnetograms are provided by the HMI (Schou et al. 2012). For the purpose of extrapolating the magnetic topology of the active region, we use a set of vector magnetograms from the Space-weather HMI Active Region Patches (SHARPs) data series with a cadence of 12 minutes.

Figure 1 gives an overall picture for the flare, the active region, and their surroundings. The flare occurred in a multipolar magnetic configuration formed by the sunspot area in the active region and an adjoining bipolar plage region to its west. By inspecting the evolution of the two active regions and the surrounding area from July 1 to 5, we find that the plage area evolved from sunspots in the active region 11514, which experienced a decay process in these days. In the active region 11515, which is classified as $\beta\gamma\delta$ type, the main sunspot is of

predominant positive polarity surrounded by satellite sunspots with scattered negative fields. Combined with the bipolar field in active region 11514, an asymmetric quadrupolar magnetic field is formed. Thus, two magnetic polarity inversion lines (PILs) are formed in this quadrupolar field. Over the two PILs lie two filaments with different sizes.

In a preceeding paper (Wang et al. 2018), we reported the evolution of three hot channels, two of them erupted successfully, pushing the overlying filament and causing its partial eruption (Filament 1, the larger one in Figure 1(a)). The eruption of the two hot channels caused two flaring sites along the PIL near the sunspot and two peaks on the GOES lightcurves (Figure 2(L1)). Here, we refer to them as main peak 1 (at $\sim 21:42$ UT) and main peak 2 (at $\sim 21:45:40$ UT), respectively. The eruption disturbs the overlying magnetic field of the plage region, producing a pair of remote secondary flare ribbons, which lie alongside filament 2 (the smaller one in Figure 1(a)). The filament is stationary between the secondary flare ribbons and remains intact throughout the flare process. Thus, we observe two pairs of flare ribbons: one pair of ribbons (main flare ribbon) associated with the main flaring site and another pair of ribbons along the PIL of the bipolar plage, the secondary flare ribbons (Zhang et al. 2014).

3. The EUV Late Phase

3.1. Three Sets of Flare Arcades

As mentioned above, we notice the flare's late phase from AIA 131 Å images, so we start with showing the AIA images. The right panels of Figure 2 display snapshots of the partial eruption of filament 1 during the flare observed in eight passbands of AIA and in 10830 Å narrowband images. From the corresponding online animation, we can see the filament's partial eruption, including subsequent contraction of filament threads. The contraction of filament threads was immediately followed by the appearance of hot loops at 131 Å. In fact, we notice three sets of flare loops appearing in turn. The contraction with a speed of 295 km s⁻¹ can be defined as a kind of backward bouncing, which created brightenings at 1600 Å. It is interesting to note that a bouncing filament thread produces a brightening X-type configuration when it meets the low-lying magnetic field (located on the lower left of the panels in AIA images in Figure 2). The X-type brightening is accompanied with plasma flows. We interpret it as magnetic reconnection produced by the contracting magnetic threads. Actually, the purpose of this paper is to demonstrate that the EUV late phase is produced through magnetic reconnection when the backward bouncing magnetic threads collide with a low-lying magnetic field.

It is worthwhile to mention that, on the GOES time profiles (Figure 2(L1)), the decay of the flare does not follow the slope of the second main peak at 21:45 UT. Instead, the flare's decay becomes much more gradual, exhibiting a kind of dual-decay behavior as defined by Woods (2014). The dual-decay behavior is a signature for the existence of EUV late phase in most circumstances. In addition, there are several noticeable gentle peaks during the gradually decaying period. When checking their origin with EUV full disk images, we find that all of them originated from other sites. For example, a peak at \sim 21:57 UT comes from a jet event from elsewhere on the solar disk. Thus, we neglect all of these gentle SXR peaks in the subsequent analysis.

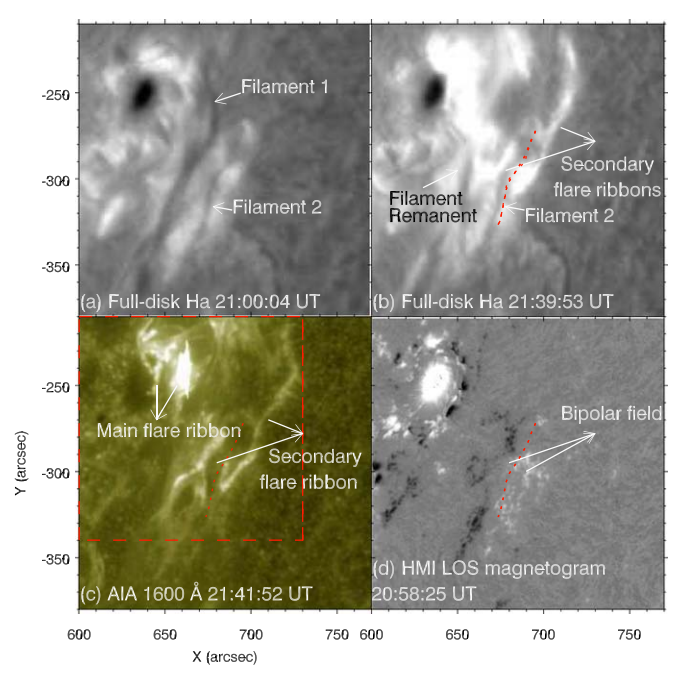


Figure 1. The morphology of the flare ribbons and the two filaments (panels (a)–(c)) as observed in BBSO full-disk ${\rm H}\alpha$ 6563 Å and AIA UV 1600 Å in the context of the photospheric LOS magnetic field observed by HMI (panel (d)). The large filament and the smaller one are labeled as filament 1 and filament 2, and the latter is depicted as red dotted curves in panels (b)–(d). The arrows in panel (d) highlight the bipolar field formed by the plages. The box with the red dashed lines in panel (c) indicates the field of view (FOV) in Figures 3, 5, and 7.

Figure 2(L2) gives the time profiles of the background-subtracted irradiance in four EVE spectral lines, which include 133 Å (Fe XX/XXIII, log $T\sim6.97$), 211 Å (Fe XIV/XII, log $T\sim6.27$), 335 Å (Fe XVI, log $T\sim6.43$), and 304 Å (He II, log $T\sim4.9$). The variabilities are obtained by subtracting the preflare irradiance at 21:00 UT. We find that there is a small bump around 22:20 UT in 335 and 211 Å. In addition, there are three noticeable peaks in the 304 Å lightcurve. The emission at 304 Å represents the chromospheric response to the energy release during the impulsive phase. However, the middle peak at 21:43 UT has no corresponding response on the GOES lightcurve.

While EVE measures the full-disk integrated EUV irradiance from all sources on the disk, we use the spatially resolved observation from AIA to derive uncontaminated profiles of the ELP emission. Figure 2(L3) gives the integrated lightcurves at seven EUV passbands observed by AIA over the FOV of the right panels. After the impulsive phase, the emission peaks first appear in the highest temperature in AIA 131 Å, and then progressively appear in increasingly cooler temperatures.

In Figure 3, the two columns in the middle show three distinct sets of loops. They are most visible at \sim 21:49 UT, \sim 22:01 UT, and \sim 22:40 UT, respectively. The loops are visible in all EUV passbands of AIA, and we label these loops as flare arcades 1, 2, and 3 (panels (a1)–(a3)). Flare arcade 1 corresponds to the main phase of the flare. The AIA 1600 Å images (panels (c1)–(c3)) allow us to identify the nature of the footpoints of these flare arcades. The footpoints of flare arcade 1 take their roots in the sunspot and surrounding satellite

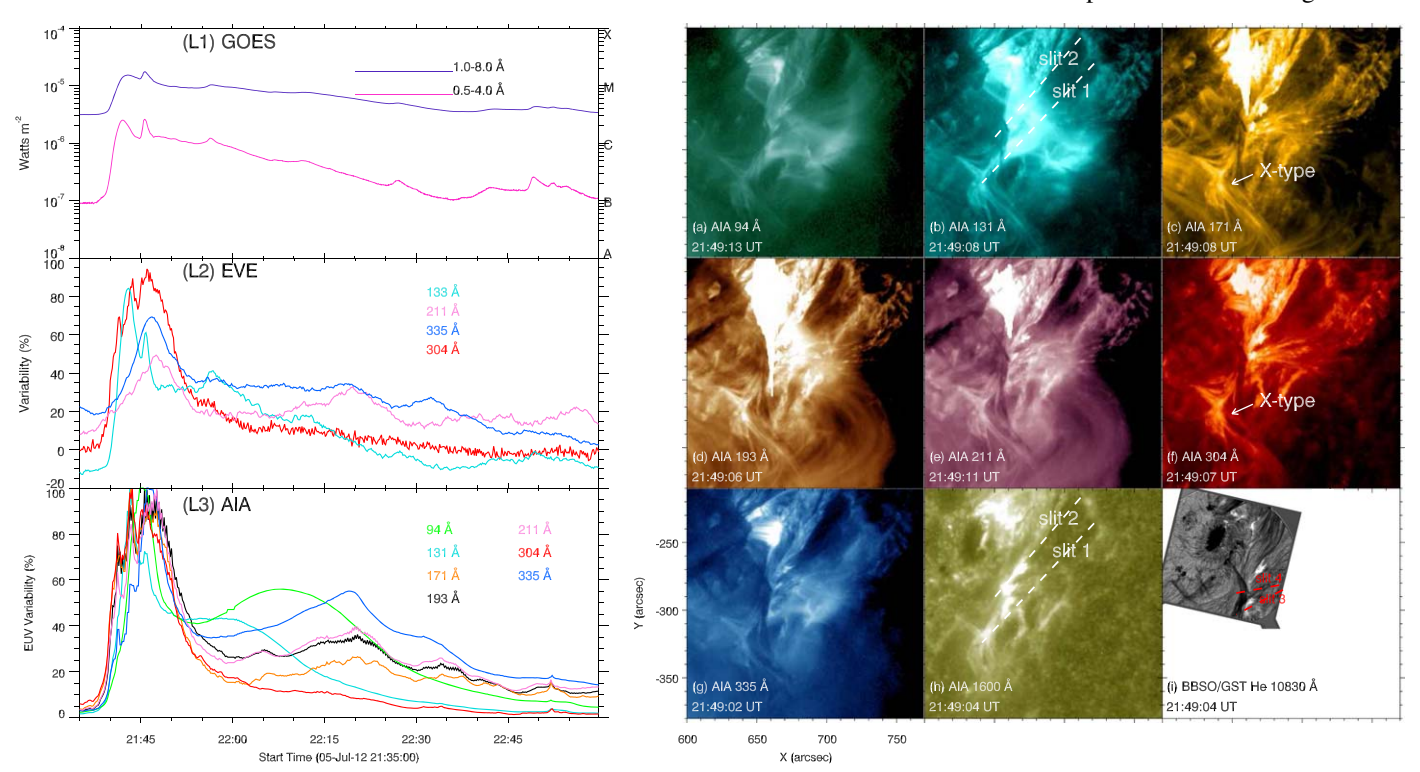


Figure 2. Online animation of the flare evolution in seven EUV passbands: 94, 131, 171, 193, 211, 304, and 335 Å, one UV passband: 1600 Å, and a chromospheric passband: 10830 Å (panels (a)–(i)). The time profiles for GOES 1–8 Å and 0.5-4 Å (panel (L1)), EVE full-disk irradiance (panel (L2)) and AIA subregion intensities integrated over the FOV of the right panels in seven lines are shown on the left. The slits 1–4 in panels ((b), (h), and (i)) indicate the position for making the spacetime diagrams in Figure 8. An animation of this figure is available, running from 21:00 to 23:00 UT. The realtime duration of the video is 59 s. (An animation of this figure is available.)

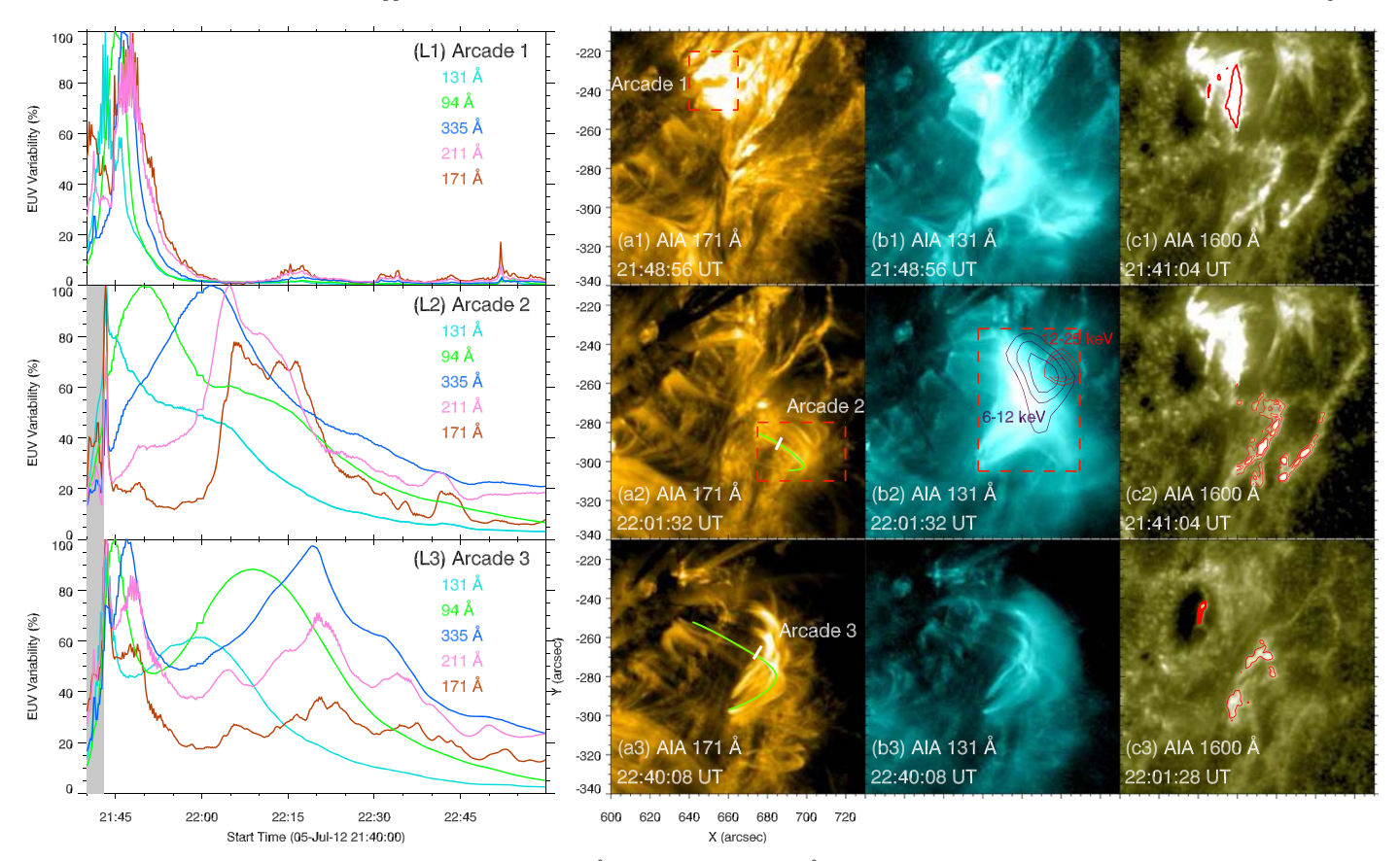


Figure 3. Snapshots of three sets of flare loops observed in AIA 171 Å (panels (a1)–(a3)), 131 Å (panels (b1)–(b3)) passbands and their footpoint emission shown as ribbons in AIA 1600 Å. The three sets of loops are labeled as arcade 1 in panel (a1), arcade 2 in panel (a2), and arcade 3 in panel (a3), respectively. Red contours are depicted to highlight footpoint emission for the three sets of flare loops. The red dotted boxes represent the integration regions of the AIA intensities shown on the left (panels (L1)–(L3)), for arcades 1, 2, and 3, respectively. While, green curves in panels (a2) and (a3) depict the lengths of arcades 2 and 3, respectively. The white short cuts on the green curves indicate the position where we fit the flux with Gaussians to obtain the loop widths. In panel (b2), SDO/AIA 131 Å image at 22:01:32 UT is overlaid with the X-ray source at 6–12 keV (purple) and 12–25 keV (red) as obtained from observation made by RHESSI.

sunspots (panels (a1)–(c1)), and the flare arcade 2 is anchored at the bipolar field configuration (panels (a2)–(c2)) in the plage area. The ribbons in the plage area are the so-called secondary flare ribbons (SFRs), while the ribbons in the sunspots are normal flare ribbons (Zhang et al. 2014). Flare arcade 3 connects the sunspot-side footpoint of arcade 1 and one footpoint (the negative branch of the bipolar field) of the arcade 2 (panels (a3)–(c3)). Their conjugate relationships, as deduced from the observed connectivities described above, are depicted with red contours in panels (c1)–(c3).

To understand how these loops are magnetically connected, we carry out nonlinear force-free field (NLFFF) extrapolation, adopting the optimization approach proposed by Wheatland et al. (2000) and implemented by Wiegelmann (2004) and Wiegelmann et al. (2006). The 180° ambiguity in the transverse components of the vector magnetic field is resolved by the improved minimum energy method (Metcalf et al. 2006; Leka et al. 2009). The adopted dimensions for the extrapolation are $160 \times 160 \times 160 \text{ Mm}^3$. The bottom boundary is from vector magnetogram at 21:00 UT. The resulting magnetic topology of the active region is shown in Figure 4. The extrapolation clearly confirms the connectivities of the three sets of magnetic arcades, as observed by AIA (Figure 3).

The time profiles of the EUV fluxes from flare arcades 1–3 are plotted in the panels (L1)–(L3) of Figure 3. They are obtained from corresponding subregions given in panels (a1), (a2), and (b2). We find that the three flare arcades appear

sequentially from 1 to 3. Their EUV emission peaks appear sequentially with decreasing temperature as well. It is apparent that the late phase emission is jointly contributed from arcades 2 and 3. For the lightcurves in panels (L2) and (L3), the emission peaks in the shaded area are from the flare's main phase. On average, the emission peak of flare arcade 3 lags behind flare arcade 2 about 15 minutes during the EUV late phase. Arcade 3 is the most prominent in AIA 131 Å images, which actually motivated us to carry out the current investigation. It is associated with X-ray emission at 6-12 and 12-25 keV, as observed by RHESSI (Lin et al. 2002). The peak time of the two flare arcades are listed in Table 1 with respect to different wavelengths. Due to contamination by light from the erupting hot channels, the start time of flare arcade 2 at 131 Å and 94 Å are unclear. Based on the time profiles, we estimate the cooling time of the two flare arcades to be about 30 and 45 minutes.

To inspect the thermal behavior of the three arcades, we applied the differential emission measure (DEM; Cheung et al. 2015; Su et al. 2018) method to six AIA coronal passbands, obtaining the emission measure maps in three different temperature bands, 1–2.5 MK, 5–8 MK, and 9–20 MK, respectively, as illustrated in Figure 5. As a result, the temperature of arcade 3 turns out to be the highest among the three arcades. Panel (f) indeed displays that the hottest emission comes from arcade 3, which reaches temperature of the order of 10 MK. During the same time (~22:00 UT), arcade

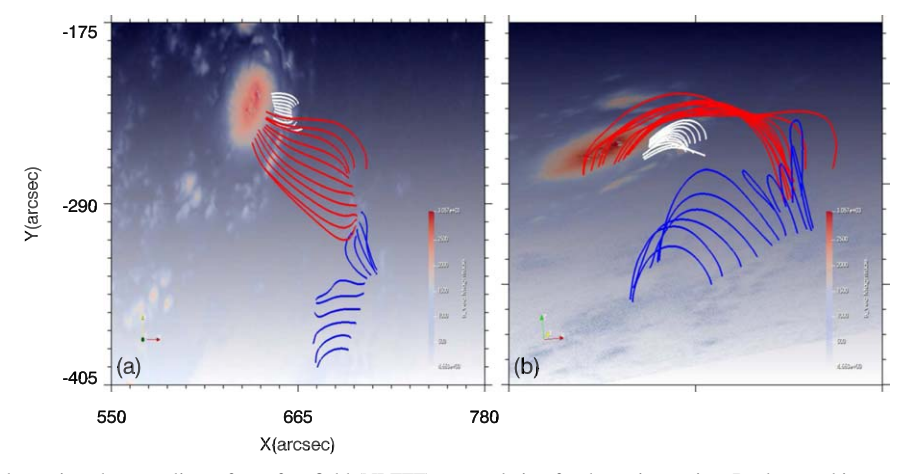


Figure 4. Magnetic field topology given by a nonlinear force-free field (NLFFF) extrapolation for the active region. Background images indicate the bottom boundary. The red portion represents positive magnetic field, while the blue portion represents negative magnetic field. The white, red, and blue solid lines indicate the magnetic field lines of the NLFFF model. Panel (a) emphasizes magnetic field topology in the *X*–*Y* plane as seen from the *Z*-direction, while panel (b) shows a three-dimensional perspective from the side view.

Table 1
Timelines of the Two Late Phase Arcades

	131 Å	94 Å	335 Å	211 Å	171 Å
Flare arcade	peak time				
2	~21:43	~21:50	~22:02	~22:05	~22:06
3	~21:59	~22:09	~22:19	~22:20	~22:20

2 has cooled down to the range between 1 and 2.5 MK. About 40 minutes later, arcade 3 cooled down, but still contains components in all temperature bins (panels (g)–(i)).

Figure 6 gives the emission measure distribution diagrams over time and temperature, which is averaged in the black box shown in Figure 5(i). The arrows indicate the increases in temperature on the top of arcade 3. We find that there is a sudden jump in temperature at 21:47 UT.

3.2. The Partial Eruption and Footpoint Emission

We have seen that the emissions from two late-phase arcades have different peak times. Flare arcade 2 strides over filament 2 observed in $H\alpha$, which remains static. At the same time, two parallel ribbons appear alongside the small filament. The parallel ribbons do not exhibit the usual separation motion. We suggest that flare arcade 2 may result from the disturbance of the overlying magnetic field when the erupting hot channels pass through the bipolar plage region.

Flare arcade 3 was obviously heated twice. Our finding is that the heating episodes are associated with the rapid contractions of filament threads during the filament's partial eruption. Figure 7 and the corresponding online animation display the brightenings at the footpoints of the arcades. In the previous section, we named the two emission peaks created by the eruption of the two hot channels in the flare main phase as peak 1 (at ~21:42 UT) and peak 2 (at ~21:45:40 UT) on the GOES lightcurve. The two peaks are closely related to the two peaks at 21:41:20 and 21:45:20 UT on the AIA 1600 Å lightcurve in Figure 7. The eruption of the first hot channel produced brightenings in the regions of "a" and "c," which correspond to the flaring sites. Subsequently, it was followed by rapid contraction of the overlying filament threads. Both

AIA 1600 Å and He I 10830 Å images show that the rebounding filament threads lead to immediate brightenings around footpoints "d" and "b" at 21:43:50 UT (peak 3) in Figure 7. Note that the aforementioned AIA 304 Å peak (~21:43 UT) in Figure 1 should be of the same origin. The second contraction of the overlying filament threads occurs immediately after the eruption of the second hot channel that produced peak 2. Both footpoints "d" and "b" have an emission peak at 21:47 UT (peak 4) as a response to the second contraction. Here, it is worth mentioning that flare arcade 3 connects the areas of footpoints "d" and "b."

The key point for the heating is the obvious filament contraction during the partial eruption observed in He I 10830 Å images. Along the direction of contraction, we plot the spacetime diagrams in 10830 Å passband along slits 3 and 4 (Figure 2(i)), indicated in Figure 8. As a result, we find two episodes of strong downward motion at 21:43:50 UT and 21:47 UT. They are corresponding to the peaks 3 and 4 on the lightcurves obtained from regions "b" and "d" in Figure 7. Simultaneously, two hot mass motions are seen in the 131 Å and 1600 Å passbands (Figure 8). In the high-resolution He I 10830 Å data, the two rapid contractions of the filament materials along slits 3 and 4 move at the speed of \sim 295 km s⁻¹. For a free falling material with zero resistance force, gaining this speed from a static state needs about 20 minutes, which is significantly longer than observed. We thus suggest the contraction of the filament is powered by a sudden unbalanced Lorentz force following a sudden magnetic pressure drop after the eruption of hot channels.

3.3. Cooling Time

The cooling processes of arcades 2 and 3 are apparent from the time profiles of SDO/AIA EUV flux variabilities (Figures 3(L2) and (L3)). The peaks of the lightcurves during the late phase sequentially appear from 131 Å (log $T\sim$ 5.6, 7.0), 94 Å (log $T\sim$ 6.8), 335 Å (log $T\sim$ 6.4), 211 Å (log $T\sim$ 6.3) to 171 Å (log $T\sim$ 5.8). Thus, the cooling time based on observation is about 30 and 45 minutes for arcades 2 and 3, respectively.

To study the cooling process, we used the model of Cargill et al. (1995), which is based on conductive and radiative cooling timescales derived from the energy transport equation

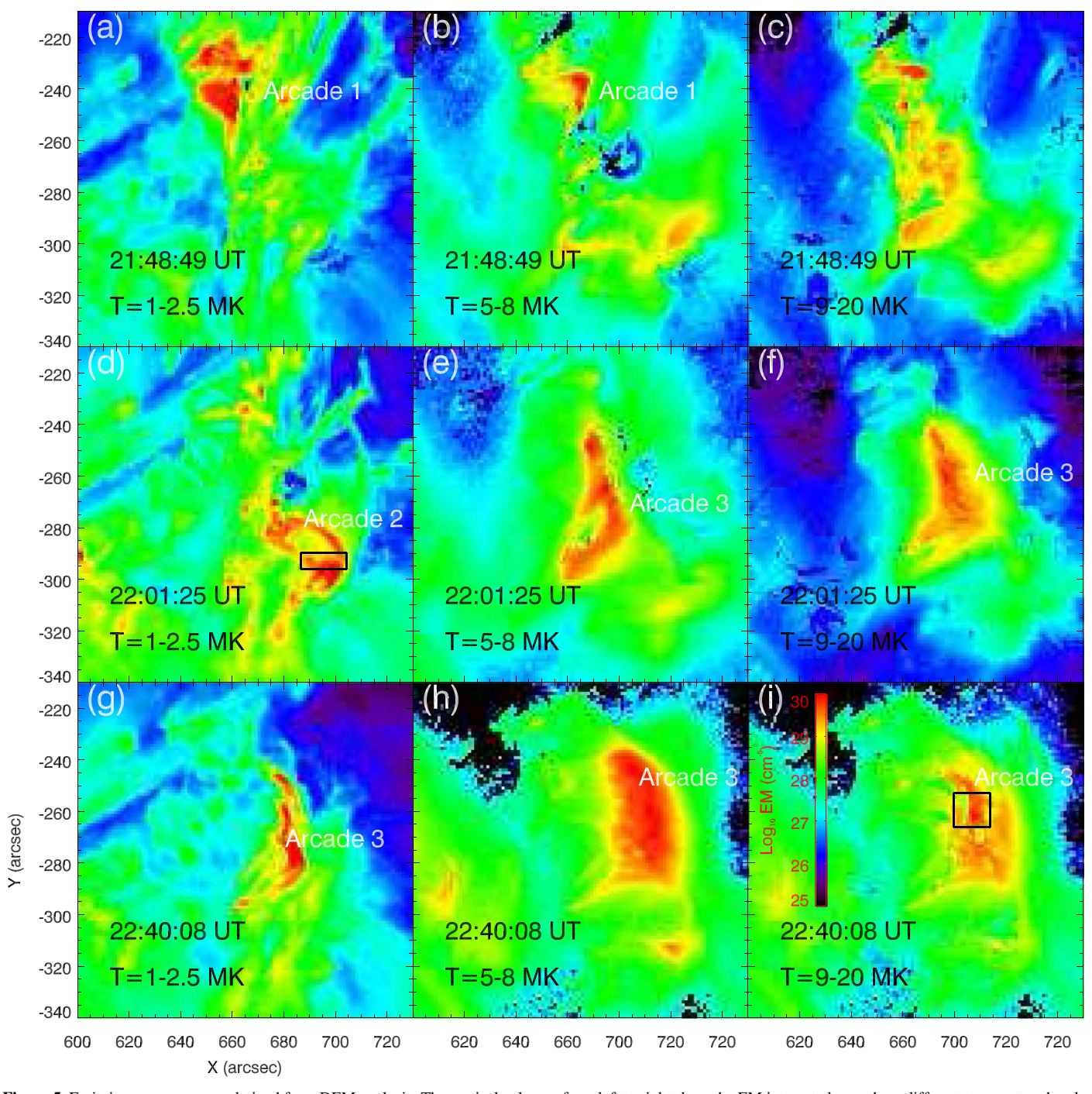


Figure 5. Emission measure maps derived from DEM analysis. The vertical columns from left to right show the EM integrated over three different temperature bands, 1–2.5, 5–8, and 9–20 MK. The rows from top to bottom are at three different times at 21:48:49, 22:01:25, and 22:40:08 UT, respectively, corresponding to the times from top to bottom in Figure 3. The boxes in panels (d) and (i) present the two regions where EM, temperature and density are calculated for the top of arcades 2 and 3, respectively.

(see Cargill 1994; Cargill et al. 1995, Ryan et al. 2013). In order to derive the characteristic timescales of the cooling mechanisms, Cargill et al. (1995) assumed that the thermal energy density is altered only by means of conductive and radiative heat flux. Based on the SDO/AIA 171 Å images, we can obtain the lengths and widths of these flare loops. The apparent loop lengths are estimated to be 27 Mm for the loop of arcade 2 and 58 Mm for the loop of arcade 3, as shown by the green curves in panels (a1) and (a3) of Figure 3. The widths (w) of arcades 2 and 3 are estimated to be 1 Mm. Also based on

their typical temperature and mass density estimated from DEM, where the density is estimated by $\sqrt{\frac{EM}{w}}$, the conductive and radiative cooling times are estimated in Table 2.

Obviously, conductive cooling dominates initially followed by radiative cooling at a later time. In this case, according to Cargill et al. (1995), the total cooling time (τ_{cooling}) is then

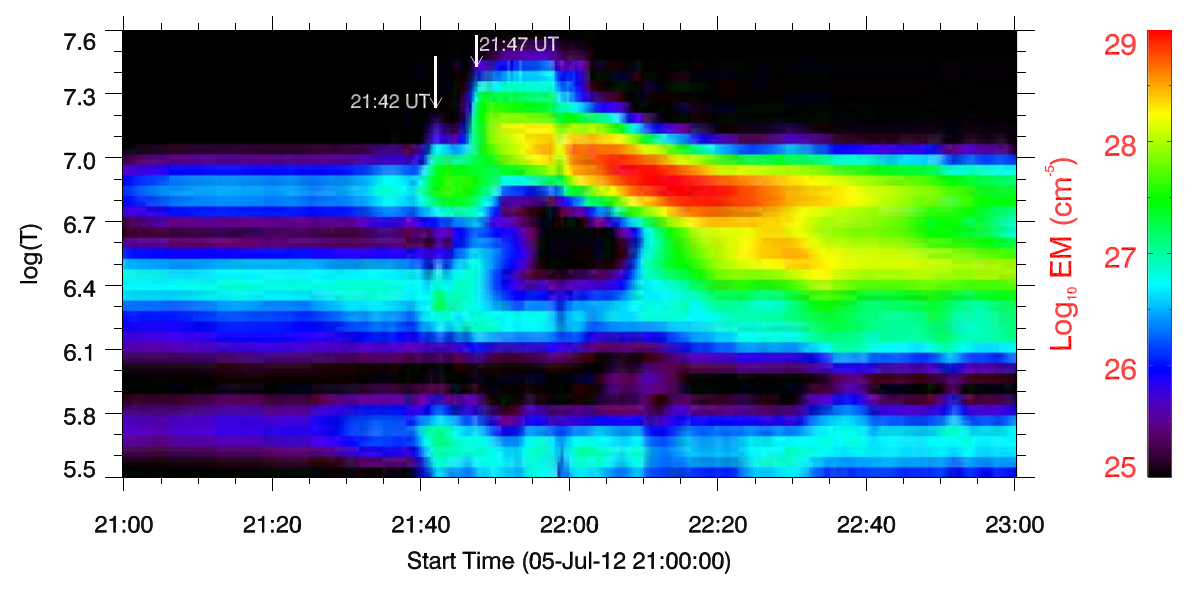


Figure 6. The emission measure distribution diagrams as a function of time and temperature, represented by the horizontal *X*-axis and vertical *Y*-axis, respectively. The arrows indicate the increases in temperature on the top of loop 3 (see the text). The EM distribution is averaged over the black box shown in Figure 5.

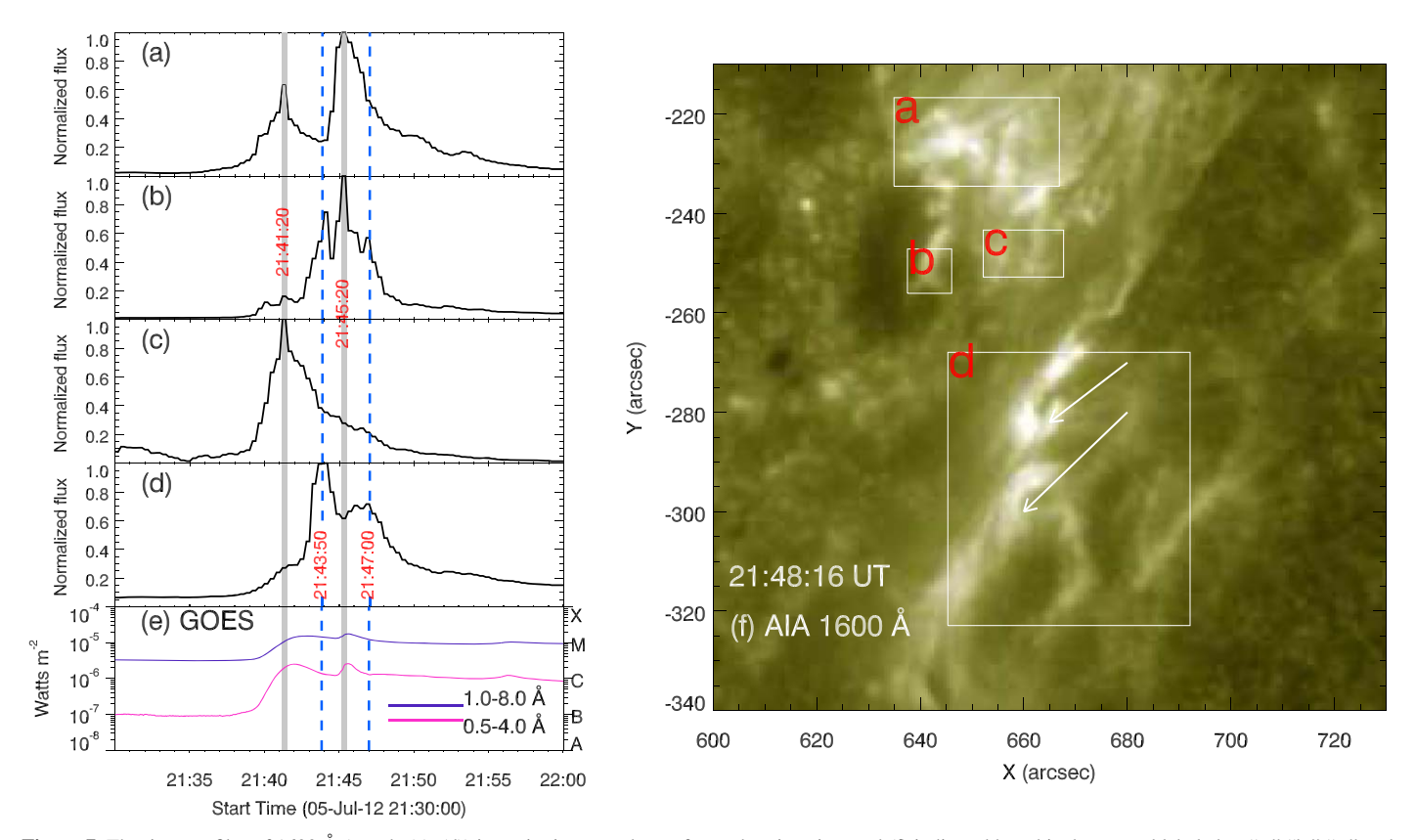


Figure 7. The time profiles of 1600 Å (panels (a)–(d)) intensity integrated over four subregions in panel (f) indicated by white boxes and labeled as "a," "b," "c," and "d," respectively. The two shaded areas indicate the two flares occurring in the main phase corresponding to two peaks on GOES lightcurves (panel (e)), while the blue dashed lines refer to the brightenings caused by the rebouncing magnetic reconnections on loop 3, occurring at \sim 21:43:50 and 21:47 UT. The two arrows in panel (f) indicate the positions of brightenings accompained by two contractions. An online animation is available, starting at 21:30 UT and ending at 21:58 UT. The realtime duration of the video is 10 s.

(An animation of this figure is available.)

estimated as

$$\tau_{\text{cooling}} = \tau_c \left[\left(\frac{\tau_r}{\tau_c} \right)^{7/12} - 1 \right] + \frac{2}{3} \tau_r \left(\frac{\tau_c}{\tau_r} \right)^{5/12} \left[1 - \left(\frac{T_L}{T_*} \right) \right],$$

where T_* is the temperature where the dominance of conductive cooling is replaced by radiative cooling, T_L is the temperature at which the single power law of the radiation loss function becomes inaccurate (Cargill et al. 1995). Assuming $T_L \ll T_*$, the total cooling times of flare arcades 2 and 3 can be

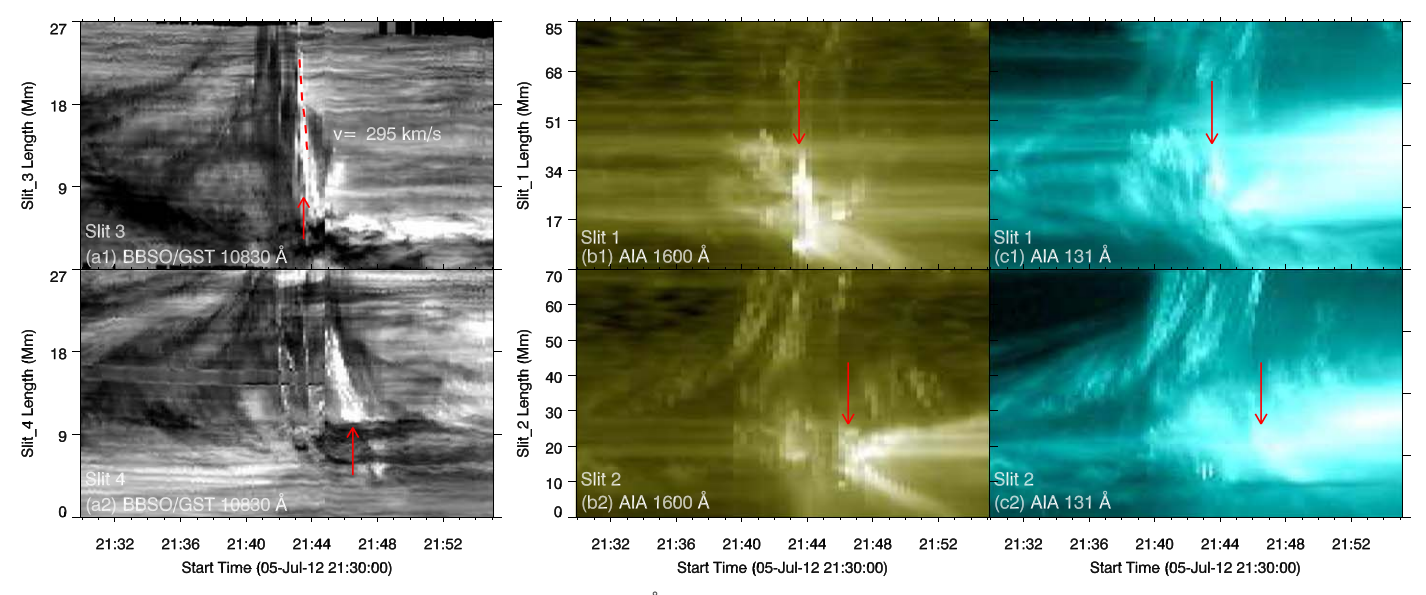


Figure 8. Spacetime diagrams obtained by stacking 10830, 1600, and 131 Å intensity images along slits 3, 4 and slits 1, 2 given in panels (i), (b), and (h) of Figure 2. The upper panels display the downward motion in 131 and 10830 Å and footpoint brightings in 1600 Å indicated by red arrows, at around 21:43 UT, while the arrows in the lower panels show the downward motion and brightings at around 21:47 UT.

 Table 2

 Cooling Timescales for the Flare Arcades in ELP

Flare Arcade	Temperature $T_{\text{max}} (10^6 \text{ K})$	Density $n (10^9 \text{ cm}^{-3})$	Length $10^9~{\rm cm}$	$ au_c$ minutes	$ au_r$ minutes	$ au_{ m cooling}$ minutes
2	12.6	46.5	2.7	1.2	155.8	17.3
3	20.0	33.5	5.8	1.3	51.9	32.9

estimated as 17 and 33 minutes. The cooling times from the Cargill et al. (1995) method are less than the observed cooling times by about 35%.

4. Conclusion and Discussion

This is our third paper on the M1.8 class flare of 2012 July 5, focusing on its EUV late phase. We identify the EUV late phase from the appearance of 131 Å emission in a separate flare arcade from the main flare arcade. The late phase can also be identified as a second peak in warm emission lines based on the SDO/EVE spectrum and SDO/AIA lightcurves. Combining the results from observations of SDO and BBSO, NLFFF modeling, DEM analysis, and estimation of cooling times, our main findings can be summarized as follows:

- (1) There are three sets of loops (arcades 1, 2, and 3) with different sizes in the entire flaring process. They are located in an asymmetric quadrupole magnetic field formed by the active region's complex sunspot and a neighboring bipolar plage. The extrapolated magnetic topology shows quite a good agreement with the morphology of three arcades based on AIA observations.
- (2) The EUV late phase emission apparently comes from a combined contribution of two separate arcades (flare arcades 2 and 3). With no doubt, they are additionally heated. The observed cooling times for the two flare arcades are longer than the theoretical expectation.
- (3) We report that the heating of flare arcade 2, linking the pair of secondary flare ribbons, is the result of disturbance made by the eruption of EUV hot channels into the overlying coronal magnetic field. The heating of flare

arcade 3 was caused by magnetic reconnection which may have occurred between the contracting filament threads and the low-lying magnetic field.

The scenario of magnetic reconnection made by contracting filament threads and low-lying magnetic fields is supported by the observation of a bouncing filament thread which produces a brightening X-type configuration and an ejection of plasma when it meets the low-lying magnetic field. This provides strong evidence for magnetic reconnection. Based on all the observational facts, we argue that magnetic reconnection might occur between the contracting filament threads and the low-lying magnetic field, which leads to the heating of arcade 3, supported by some observational facts, such as the brightenings of the footpoints of flare arcade 3 having peaks at 21:43:50 UT and 21:47 UT. The temperature of arcade 3 had an abrupt increase at 21:47 UT, also indicating the heating. It is also worth mentioning that there is a failed eruption of a hot channel, but we find no evidence of heating by this hot channel.

The conclusions support the statistical results obtained by Wang et al. (2016b), which revealed that the relative peaks of the noneruptive flares are systematically stronger than those eruptive flares (Dai et al. 2018b). In noneruptive flares, there should be more magnetic threads contracting back. However, the flare analyzed in this paper is definitely of eruptive nature, but the partial eruption overlaps with the nature of confined (or failed) eruption (Ji et al. 2006; Shen et al. 2014; Dudík et al. 2016). In addition, contraction of flare loops or peripheral loops is common in most eruptive flares. Also nearly all eruptive flares are followed by material falling back. It would be interesting to investigate the role of contracting loops,

especially the falling material, in flares' late phase emission, with more well observed events.

We thank the team of SDO/AIA and SDO/HMI for providing the valuable data. The AIA and HMI data are downloaded via the Virtual Solar Observatory and the Joint Science Operations Center. We thank Yang Su and Thomas Wiegelmann for sharing the DEM and NLFFF codes, respectively. This work is supported by NSFC grants 11790302 and 11729301. Y.W. is supported by NSFC 12003072 and the Youth Fund of Jiangsu No. BK20191108. The work of A.W. was supported by DLR under grant No. 50 QL 1701. This work is also supported by the Strategic Priority Research Program on Space Science, CAS, grant No. XDA15052200 and No. XDA15320301.

ORCID iDs

Ya Wang https://orcid.org/0000-0003-3699-4986 Ying Li https://orcid.org/0000-0002-8258-4892

References

```
Cargill, P. J. 1994, ApJ, 422, 381
Cargill, P. J., Mariska, J. T., & Antiochos, S. K. 1995, ApJ, 439, 1034
Chen, J., Liu, R., Liu, K., et al. 2020, ApJ, 890, 158
Cheung, M. C. M., Boerner, P., Schrijver, C. J., et al. 2015, ApJ, 807, 143
Dai, Y., & Ding, M. 2018a, ApJ, 857, 99
Dai, Y., Ding, M., Zong, W., et al. 2018b, ApJ, 863, 124
Dai, Y., Ding, M. D., & Guo, Y. 2013, ApJL, 773, L21
```

```
Donnelly, R. F., & Kane, S. R. 1978, ApJ, 222, 1043
Dudík, J., Polito, V., Janvier, M., et al. 2016, ApJ, 823, 41
Fletcher, L., Dennis, B. R., Hudson, H. S., et al. 2011, SSRv, 159, 19
Goode, P. R., Coulter, R., Gorceix, N., Yurchyshyn, V., & Cao, W. 2010, AN,
  331, 620
Hock, R. A., Woods, T. N., Klimchuk, J. A., Eparvier, F. G., & Jones, A. R.
  2012, arXiv:1202.4819
Ji, H., Huang, G., Wang, H., et al. 2006, ApJL, 636, L173
Kane, S. R., & Donnelly, R. F. 1971, ApJ, 164, 151
Leka, K. D., Barnes, G., Crouch, A. D., et al. 2009, SoPh, 260, 83
Lemen, J. R., Title, A. M., Akin, D. J., et al. 2012, SoPh, 275, 17
Li, Y., Ding, M. D., Guo, Y., & Dai, Y. 2014, ApJ, 793, 85
Lin, R. P., Dennis, B. R., Hurford, G. J., et al. 2002, SoPh, 210, 3
Liu, K., Wang, Y., Zhang, J., et al. 2015, ApJ, 802, 35
Liu, K., Zhang, J., Wang, Y., & Cheng, X. 2013, ApJ, 768, 150
Metcalf, T. R., Leka, K. D., Barnes, G., et al. 2006, SoPh, 237, 267
Pesnell, W. D., Thompson, B. J., & Chamberlin, P. C. 2012, SoPh, 275, 3
Priest, E. R., & Forbes, T. G. 2002, A&ARv, 10, 313
Ryan, D. F., Chamberlin, P. C., Milligan, R. O., et al. 2013, ApJ, 778, 68
Schou, J., Scherrer, P. H., Bush, R. I., et al. 2012, SoPh, 275, 229
Shen, J., Zhou, T., Ji, H., et al. 2014, ApJ, 791, 83
Su, Y., Veronig, A. M., Hannah, I. G., et al. 2018, ApJL, 856, L17
Sun, X., Hoeksema, J. T., Liu, Y., et al. 2013, ApJ, 778, 139
Wang, Y., Su, Y., Hong, Z., et al. 2016a, ApJ, 833, 250
Wang, Y., Su, Y., Shen, J., et al. 2018, ApJ, 859, 148
Wang, Y., Zhou, Z., Zhang, J., et al. 2016b, ApJS, 223, 4
Wheatland, M. S., Sturrock, P. A., & Roumeliotis, G. 2000, ApJ, 540, 1150
Wiegelmann, T. 2004, SoPh, 219, 87
Wiegelmann, T., Inhester, B., & Sakurai, T. 2006, SoPh, 233, 215
Woods, T. N. 2014, SoPh, 289, 3391
Woods, T. N., Eparvier, F. G., Hock, R., et al. 2012, SoPh, 275, 115
Woods, T. N., Hock, R., Eparvier, F., et al. 2011, ApJ, 739, 59
Zhang, J., Li, T., & Yang, S. 2014, ApJL, 782, L27
```